Research Square

Preprints are preliminary reports that have not undergone peer review.
They should not be considered conclusive, used to inform clinical practice,
or referenced by the media as validated information.

Staphylococcus aureus PSMα1 amyloid structure is modulated by buffer and salt

Emilie Buhl Plechinger
Aarhus University
Kasper Holst Hansen
Aarhus University
Qian Liu
Aarhus University
Ümit Akbey
University of Pittsburgh
Maria Andreasen
mariaj@biomed.au.dk

Aarhus University

Article

Keywords: Functional amyloids, Protein aggregation, Phenol-soluble modulins, Aggregate polymorphism

Posted Date: March 19th, 2026

DOI: https://doi.org/10.21203/rs.3.rs-8956596/v1

License: This work is licensed under a Creative Commons Attribution 4.0 International License.
Read Full License

Additional Declarations: No competing interests reported.

Version of Record: A version of this preprint was published at Scientific Reports on October 7th, 2026.
See the published version at https://doi.org/10.1038/s41598-026-74007-3.

Staphylococcus aureus PSMα1 amyloid structure is modulated by buffer and salt

Emilie Buhl Plechinger[1], Kasper Holst Hansen[1], Qian Liu[1], Ümit Akbey[2] and Maria Andreasen[1*]

[1]Department of Biomedicine, Aarhus University, Aarhus, Denmark
[2]Department of Structural Biology, School of Medicine, University of Pittsburgh, Pittsburgh, PA, 15261, USA

[*]Corresponding author:
Maria Andreasen, Department of Biomedicine, Aarhus University, Høegh-Guldbergs Gade 10, 8000 Aarhus, Denmark
Tel: +45 24211421
Email: mariaj@biomed.au.dk

Keywords: Functional amyloids, Protein aggregation, Phenol-soluble modulins, Aggregate polymorphism

Abstract:

Amyloid fibrils share a characteristic cross-β structure yet often display pronounced polymorphism, where a single protein or peptide sequence can adopt multiple distinct fibrillar architectures. Environmental factors such as buffer composition, ionic strength, and pH strongly influence amyloid assembly, modulating fibril morphology, stability, and function. In *Staphylococcus aureus*, phenol-soluble modulins (PSMs) are key contributors to biofilm integrity and pathogenicity, with PSMα1 forming stable fibrils that reinforce the biofilm matrix. However, the influence of the physicochemical environment on PSMα1 aggregation remains poorly defined. Here, we systematically examine how solution conditions, ionic strength, and cross-seeding modulate PSMα1 fibril formation. Our results show that variations in these parameters markedly alter aggregation kinetics, fibril morphology, hydrophobic surface exposure, and molecular organization. Distinct buffer conditions promote the emergence of different fibrillar polymorphs, reflecting the environmental sensitivity observed in disease-associated amyloids. These findings underscore the critical role of the solution environment in directing amyloid assembly pathways and suggest that environmentally driven fibril polymorphism may contribute to *S. aureus* biofilm stability and pathogenic behavior.

Introduction:

Aggregated proteins in the form of amyloids are traditionally associated with the pathology of numerous diseases, including neurodegenerative disorders such as Alzheimer's and Parkinson's diseases, type 2 diabetes, and systemic amyloidosis[1-4]. However, not all amyloids are detrimental or linked to disease[5]. Many organisms, including bacteria, produce functional amyloids that have beneficial purposes and play essential roles in biological processes for the organism producing them[5,6]. These functional amyloids participate in processes such as structural support for biofilm matrices, facilitating long-term memory in *Drosophila*, melanin biosynthesis, and peptide hormone storage[5,7-9]. Although functional amyloids share structural similarities with disease-associated amyloids, such as the characteristic cross-β architecture with individual β-sheets oriented perpendicular to the fibril axis, they exhibit no toxicity or pathological effects in the organisms that produce them[5,10-12]. A notable example of functional amyloids is found in *Staphylococcus aureus,* a pathogen known for its biofilm-associated infections[13]. The bacterium utilizes functional amyloids to assemble and reinforce its biofilm, forming a protective barrier that enables it to evade antibiotics and host immune responses, thereby contributing to the persistence of infections[5,13]. Within the biofilm, *S. aureus* synthesizes and secretes phenol-soluble modulins (PSMs), a group of seven small peptides, namely PSMα1-4 (20-25 amino acids), PSMβ1-2 (44-45 amino acids), and δ-toxin (34 amino acids)[14-16]. All PSM peptides are small amphipathic α-helical monomers capable of self-assembling into functional amyloids[15,16]. In their monomeric form, PSMs exhibit a variety of biological functions, including cell lysis of mammalian cells or other bacterial species, interaction with cell membrane lipids, antimicrobial activity, and facilitating biofilm disassembly[12,13,16-21]. Upon aggregation, PSM peptides form typical cross-β amyloid fibril structures, which enhance biofilm integrity, rendering it resistant to mechanical stress, and enzymatic degradation, and promoting degradation of β-lactam

antibiotics[13,22,23]. Interestingly, while most PSMs form cross-β fibrils, PSMα3 assembles into a unique cross-α amyloid structure[13].

Among the PSMs, PSMα1, a 21-residue peptide (MGIIAGIIKVIKSLIEQFTGK), stands out for its ability to accelerate the aggregation of all *S. aureus* PSMs through cross-seeding mechanisms, making it a central target for disrupting *S. aureus* biofilms[13,24]. Previous X-ray micro-crystallography studies of short PSMα1 fragments demonstrated that these fragments form cross-β fibrils stabilized by a steric zipper, where tightly interlocking side chains from paired β-sheets provide structural integrity[6]. However, our recent cryo-electron microscopy (Cryo-EM) investigation of full-length PSMα1 fibrils revealed the absence of the steric zipper in the full-length fibril[25]. Instead, the full-length fibril is stabilized by inter-layer hydrogen bonding between cross-b strands. hydrogen bonding between residues involving out-of-plane β1 and β3 strands, and hydrophobic interactions between non-aromatic amino acids with short side chains such as alanine and isoleucine at the β1 strands of two PSMa1 subunit within the hydrophobic inter-protofilament interface[25]. The Cryo-EM also highlighted multiple polymorphic forms of the PSMα1 fibril, with one dominant fibril form accounting for 37% of the total fibril mass and five minor variants[25]. This most prevalent PSMα1 fibril is a left-handed U-shaped cross-β structure, made of monomers that consist of three short β-strands: β1 (residues 2 to 5), β2 (residues 7 to 11), and β3 (residues 14 to 19) that spiral around the helical axis[25]. These monomers stack in layers, forming two symmetric protofilaments exhibiting C_2-symmetry that together create the complete narrow helical fibril[25]. During the fibril assembly, diverse structural outcomes can occur, highlighting the polymorphic nature of amyloid, each contributing differently to the biological function or pathological potential of the amyloid[26-31].

The physiochemical environment, particularly buffer composition significantly influences the assembly and structural properties of PSM amyloids and causes single peptide sequence to form fibrils with diverse morphologies[26-34]. Buffer conditions influence ionic strength, the hydrophobic environment and the availability of specific ions, which affect electrostatic interactions, hydrophobic interactions and charge distributions within the peptides[26-34]. Different buffers have also been shown to directly influence the aggregation propensity through modulation of the aggregation propensity of intermediate species[35]. Furthermore, molecular motion is also buffer dependent since adsorption of buffer molecules to the protein surface modulates the protein surface charge and hence also intermolecular interactions[36]. These factors drive the formation of polymorphic fibril structures in PSM peptides ranging from straight thick fibrils to twisted, spiral, or nanotubular forms[31,37,38]. In particular, the choice of buffer can modulate fibril stability, compactness and morphology, influencing their biological functions[31,37,38]. For example, buffer with high ionic strength may stabilize compact fibril arrangements, while low ionic strength or hydrophilic environments can promote more disordered assemblies[39]. These structural changes have significant implications for the role of PSM amyloids in biofilm stability, membrane interactions and overall pathogenicity of *S. aureus*[26,32-34,40,41]. Research on PSMα3 has shown that buffer composition and salt concentration influence fibril height, shape, and twisting, ranging from thick fibrils to spiral-shaped or nanotubular structures[37,38]. Such polymorphs emerge due to alterations in the physio-chemical environment, which modify the charge distribution and hydrophobic interactions within the amyloids[31,40,42,43]. These changes drive the formation of distinct protofilaments under varying conditions, impacting fibril morphology and potentially influencing biofilm stability and pathogenicity[31,40,42,43]. Despite

advances in understanding PSMα3 polymorphism, the physio-chemical environment factors influencing PSMα1 fibril formation remain poorly understood. Understanding how changes in the physio-chemical environment such as buffers and salt concentrations influence PSMα1 polymorphism is important to understand the complex mechanisms behind amyloid formation in *S. aureus*. Such insight could provide strategies to target biofilm-associated infections by disrupting amyloid assembly.

Results

Buffer conditions influence PSMα1 fibril formation and the resulting morphology

To examine the influence of different solution conditions on PSMα1 aggregation, we monitored the aggregation kinetics of monomeric PSMα1 peptide using Thioflavin T (ThT) fluorescence assay in four different solution conditions: namely MQ-water, KPO_4, Tris and HEPES, respectively. ThT fluorescence assay revealed major differences in the aggregation kinetics of PSMα1 peptide for the four solution conditions (Figure 1A, Figure S1). Tris and KPO_4 buffers accelerated the aggregation kinetics, with Tris displaying the fastest kinetics, compared to MQ-water as has previously been used[24,25]. In Tris buffer, the aggregation half-time ($\tau_{½}$) was 21 ± 0.03 h, indicating a rapid onset of fibril formation compared to the other buffers (Figure S2A). Fibrils formed in KPO_4 had a longer half-time of 32 ± 0.98 h, suggesting a slower aggregation onset compared to Tris but faster than other solution conditions. In contrast, aggregation in HEPES was significantly slower with an extended lag phase and a reduced elongation slope, indicating slower fibril growth. However, the aggregation process in HEPES did not plateau within the experimental timeframe of 140 h. Aggregation in MQ-water proceeded at an intermediate rate with a half-time of 34 ± 1.98 h (Figure S2A). Interestingly, at low PSMα1 concentrations in KPO_4, no detectable ThT signal was observed (Figure S1), however TEM imaging confirmed the presence of aggregates. This suggests that aggregates formed in KPO_4 are either less ThT-reactive or that less aggregates formed under these conditions.

Fibrils formed in different solution conditions also display differences in exposed hydrophobic surface area as observed by ANS fluorescence (Figure 1B, Figure S2B). The quantum yield of ANS in aqueous solutions is low but increases significantly, accompanied by a blue-shift of the peak wavelength (λ_{max}), upon binding to assessable hydrophobic patches on protein surfaces[44]. The peak fluorescence intensity varied depending on the solution conditions. Fibrils formed in Tris-buffer exhibited the highest peak intensity at a blue shifted λ_{max} (505 nm), indicating a greater extent of exposed hydrophobic patches (Table S1). In contrast, fibrils formed in KPO_4 showed the lowest fluorescence intensity at red shifted wavelength (525 nm), indicating lower exposure of hydrophobic patches on the surface of the fibrils (Figure 1B). Fibril formed in MQ-water and HEPES displayed intermediate intensities with MQ fibrils displaying a slight blue shift in λ_{max} compared to those formed in HEPES. These results highlight the role of buffer conditions in modulating the accessibility of hydrophobic patches on the surface of PSMα1 fibrils. In contrast to fibrils, monomers dissolved in both MQ-water and KPO_4 showed peak intensities at 492 nm, while monomers in Tris peaked at 498 nm, with no blue shift observed for monomers in Tris (Figure S2B, Table S1). Notably, the fluorescence intensity of monomers in Tris was significantly higher than in other solution conditions, suggesting that the Tris buffer promotes a conformation with increased exposure of hydrophobic

surfaces. Monomers dissolved in KPO_4 displayed a red-shifted λ_{max} at 493 nm, mirroring the trend observed for fibrils. Interestingly, monomers formed in HEPES exhibited a blue-shifted λ_{max} (478 nm), deviating from the pattern seen for fibrils in HEPES (Figure 1B, Figure S2B, Table S1).

The structural changes of PSMα1 monomers and fibrils formed under various buffer conditions were further monitored using synchrotron radiation circular dichroism (SRCD) spectroscopy (Figure 1C, 1D). Monomeric PSMα1 showed distinct differences in SRCD spectrum indicating different secondary structures are adopted when the monomeric peptide is exposed to different solution conditions (Figure 1C). Monomers in MQ-water and Tris exhibited a spectrum with double minima at 208 nm and 221 nm, characteristic of an α-helical structure. In contrast, monomers in HEPES and KPO_4 displayed a single minimum at ~224-226 nm (Figure 1C). Deconvolution of the SRCD spectra further confirms the differences in secondary structure seen for the monomers in different solution conditions (Figure 1E, Table S2). Monomers in MQ-water and Tris buffer display ~86% α-helical structure with no significant contribution form β-sheet structure (Figure 1C, 1E, Table S2). This is in good agreement with the structure for monomeric PSMα1 previously found in MQ-water[24,45]. Interestingly, monomers in HEPES and KPO_4 display 46% and 56% α-helical structure and 13% and 10% contribution from β-sheet structure, respectively. Hence, the predominant structural content of monomers formed in HEPES and KPO4 remain α-helical (Figure 1C, 1E). This observation aligns with ANS fluorescence assay, where monomers in Tris and MQ-water exhibit similar λ_{max} (483 nm) and peak intensities at 483 nm, whereas those formed in KPO_4 and HEPES display distinct differences in terms of peak intensity. Upon aggregation in the different solution conditions, the SRCD spectra revealed shift to a predominant β-sheet structure in all solution conditions, with single minimum observed at 218nm for MQ-water and Tris, 219 nm for KPO_4, and 216nm for HEPES, respectively (Figure 1D). Deconvolution of the SRCD spectra revealed that β-sheets accounted for 36% and 33% of the spectra in MQ-water and Tris, respectively (figure 1E). The shift from predominantly α-helical to predominantly β-sheet structure upon aggregation has also been previously reported for PSMα1 when aggregation occurs in MQ-water[24,25]. Unordered structures contributed with ~30-32%, while α-helices accounted for ~23-25%. In HEPES fibrils, α-helices (34%), and unordered structures (33%) were the major components, with β-sheets accounting for 24%. In contrast, KPO_4 fibrils nearly equivalent contributions were seen from unordered structures, α-helices and β-sheets contributing with ~30% each. These finding suggest that β-sheets are a predominant structural component in PSMα1 fibrils regardless of the solution conditions, however the solution conditions significantly influence the balance between α-helices, β-sheets, and unordered structures seen in the aggregates (Figure 1D, 1E).

Solution conditions influence cell toxicity and catalytic activity of PSMα1 fibrils

The cytotoxicity of PSMα1 monomers and fibrils formed under different buffer conditions was investigated using the lactate dehydrogenase (LDH) release assay (Figure 1E). In agreement with ANS fluorescence data and SRCD analysis, differences in cytotoxicity were observed for PSMα1 fibrils formed at different solution conditions. This indicates that the differences observed in structure are relevant for the membrane interaction pattern of the aggregates. For PSMα1 monomers a notable variation in secondary structure was observed across all the solution conditions. Based on these structural differences, a corresponding difference in cytotoxicity might be expected. However, no

significant differences in monomer cytotoxicity were observed, with cell death rates consistently around ~20% regardless of the buffer (Figure 1E). Interestingly, in Tris and KPO_4 buffer, the monomers exhibited a higher cytotoxicity than the corresponding fibrils. This trend aligns with similar observations reported for PSMα1 and PSMα3 in previous studies[10,25].

Fibrils formed in MQ-water exhibited the highest cytotoxicity (32% cell death, $p<0.05$), while fibrils formed in Tris and KPO_4 buffers exhibited the lowest cytotoxicity with cell death rates of ~14-16%. Interestingly, these results contrast with hydrophobicity measurements obtained from ANS fluorescence assay. Fibrils formed in Tris buffer exhibited the highest ANS fluorescence intensity, indicating the presence of the most accessible hydrophobic surface. Based on this observation, Tris fibrils would be expected to interact more strongly with cell membranes and, therefore, exhibit the highest cytotoxicity. However, the opposite was observed, namely Tris fibrils were among the least cytotoxic. This disparity highlights that while the hydrophobic surfaces detected by ANS fluorescence may suggest potential interaction opportunities with cell membranes, these properties do not directly correlate with cytotoxic effects and hence membrane interaction through the expose hydrophobic patches may not lead to membrane disruption and cytotoxicity. This is based on the two assays capturing different aspects of fibril behavior: ANS fluorescence measures hydrophobic exposure, while the LDH assay evaluates the biological outcome of fibril-membrane interactions. Furthermore, fibrils formed in MQ-water were significantly more cytotoxic than monomers ($p<0.05$), while no such difference were observed in KPO_4, Tris or HEPES ($p>0.05$) (Figure 1E). These findings emphasize that the physicochemical environment during fibril formation influences not only the structural and hydrophobic properties of PSMα1 fibrils but also their biological activity.

It has recently been shown that αPSMs are capable of catalyzing hydrolysis of β-lactam in antibiotics[46]. To investigate if the difference seen in PSMα1 fibrils formed under different solution conditions translate into differences in catalytic activity, we assessed their ability to hydrolyze nitrocefin, a widely used β-lactam surrogate of penicillin. Difference in catalytic activity between fibrils formed in different solution conditions were observed ($p<0.0001$), indicating that the physiochemical environment during fibril formation substantially influences their catalytic potential.

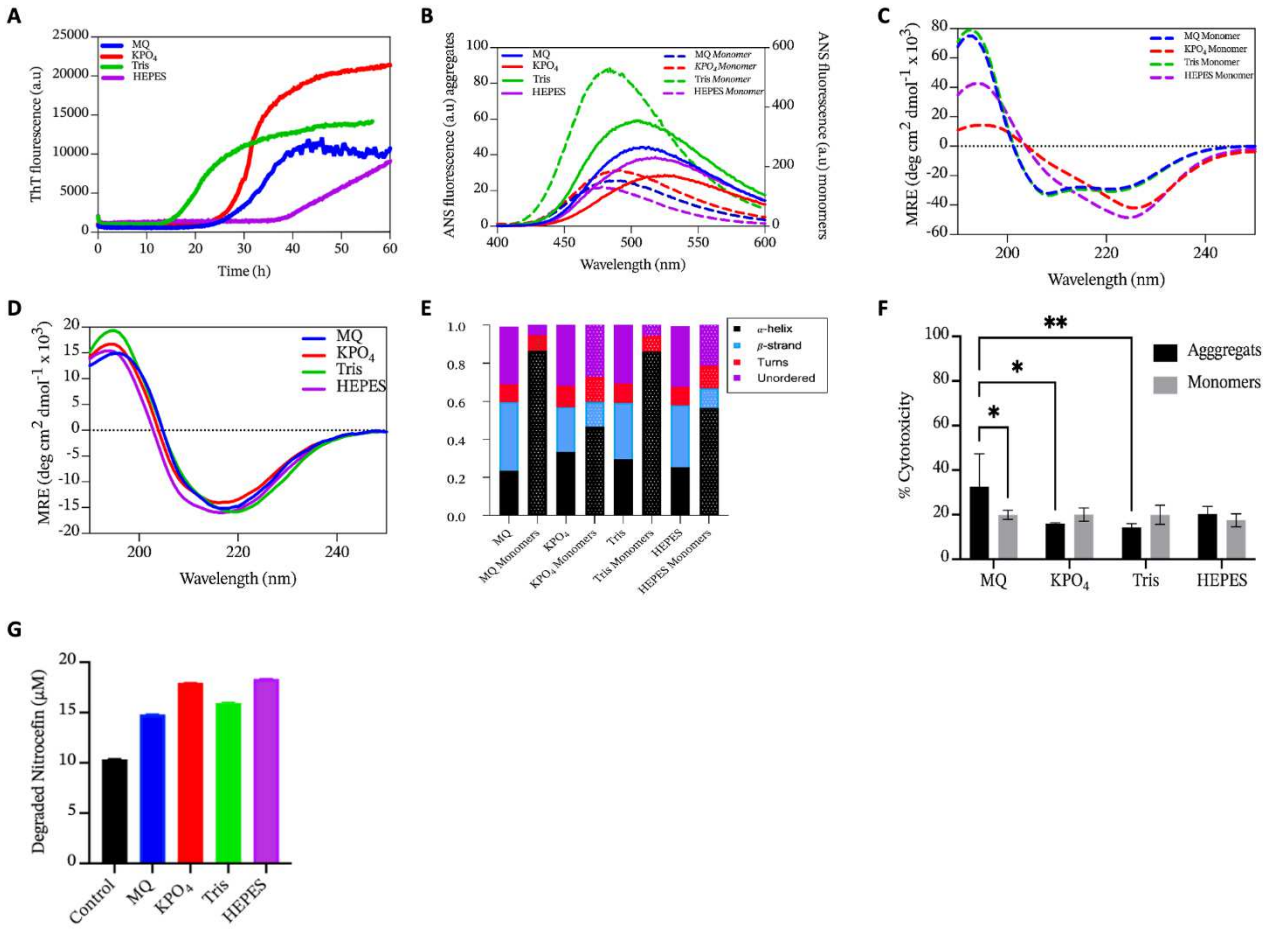


Figure 1. Solution conditions affect the aggregation kinetics and structural properties of the aggregates formed. (**A**) ThT fluorescence aggregation kinetics of PSMα1peptides (1 mg/mL) in different solutions (HEPES, Tris, KPO_4, and MQ-water) under quiescent conditions. (**B**). Left y-axis: ANS fluorescence of PSMα1fibrils in different buffer environments. Right y-axis: ANS fluorescence of PSMα1 monomers in different buffer environments. (**C**) Synchrotron radiation (SR) far UV-CD spectra of PSMα1 monomers in various buffers. (**D**) Synchrotron radiation (SR) far UV-CD spectra of PSMα1 fibrils in various buffers. (**E**) Deconvolution of the SRCD spectra of PSMα1 monomers and fibrils formed in different solutions. (**F**) Cytotoxicity of PSMα1 monomers and fibrils in different solutions. Statistical significance was determined using two-way ANOVA. *$p < 0.05$, **$p< 0.01$ (**G**) Hydrolysis of nitrocefin by PSMα1 fibrils from different solution conditions. Statistical significance was determined using one-way ANOVA, revealing a significant difference between all solution conditions ($p<0.0001$).

Buffer conditions alter the morphology of PSMα1 fibrils

The morphology of PSMα1 fibrils formed under various solution conditions was examined using transmission electron microscopy (TEM) and atomic force microscopy (AFM) (Figure 2A and 2B). Distinct morphological characteristics were observed for fibrils depending on the solution environment, highlighting the influence of the physiochemical environment during fibril formation. Fibrils formed in MQ-water were long, unbranched, and thin with an average diameter of 9.7 ± 2.6 nm. These fibrils exhibited a classic PSMα1 morphology as previously reported[24,25]. In contrast, fibrils formed in Tris and HEPES displayed a more heterogeneous morphology. These buffers produced a mixture of thin, classic fibrils (14 ± 4 nm), and wider, ribbon-like fibrils with a diameter of ~115 nm to 125 nm ± 29 nm. Interestingly some of the wider fibril appeared to wrap around other

thinner fibrils, seemingly "embracing" them (Figure 2A, black arrows). This unique feature suggests that protein interactions in these buffers promote structural rearrangements that deviate from the typical morphology observed in MQ-water. Additionally, amorphous aggregates were present in both buffers, indicating the possibility of the presence of more than one aggregation pathway. The most striking morphological differences were observed in fibrils formed in KPO_4 buffer. These fibrils were thicker and created a ribbon-like structure with diameters reaching 121 ± 13 nm, assembling into nanotubes. A unique feature of these fibrils was a twisting pattern, characterized by periodic turns along their length (Figure 2A, blue arrow), resembling one aggregate wrapping around another. In KPO_4 buffer, almost no evidence of thin, classic PSMα1 morphology was observed and only a few amorphous aggregates were observed. To further investigate the structural properties of the fibrils, AFM was used on fibrils formed in KPO_4 buffer (Figure 2B). AFM images confirmed the ribbon-like morphology and twisting appearance of KPO_4 fibrils seen in TEM images. Based on AFM analysis, the fibril is approximately 5 nm, and the periodicity of the twist is ~425 nm. Together, these observations point to a distinct aggregation pathway in KPO_4 buffer, leading to the formation of thicker, twisted fibrils rather than the typical thin morphology observed in MQ-water.

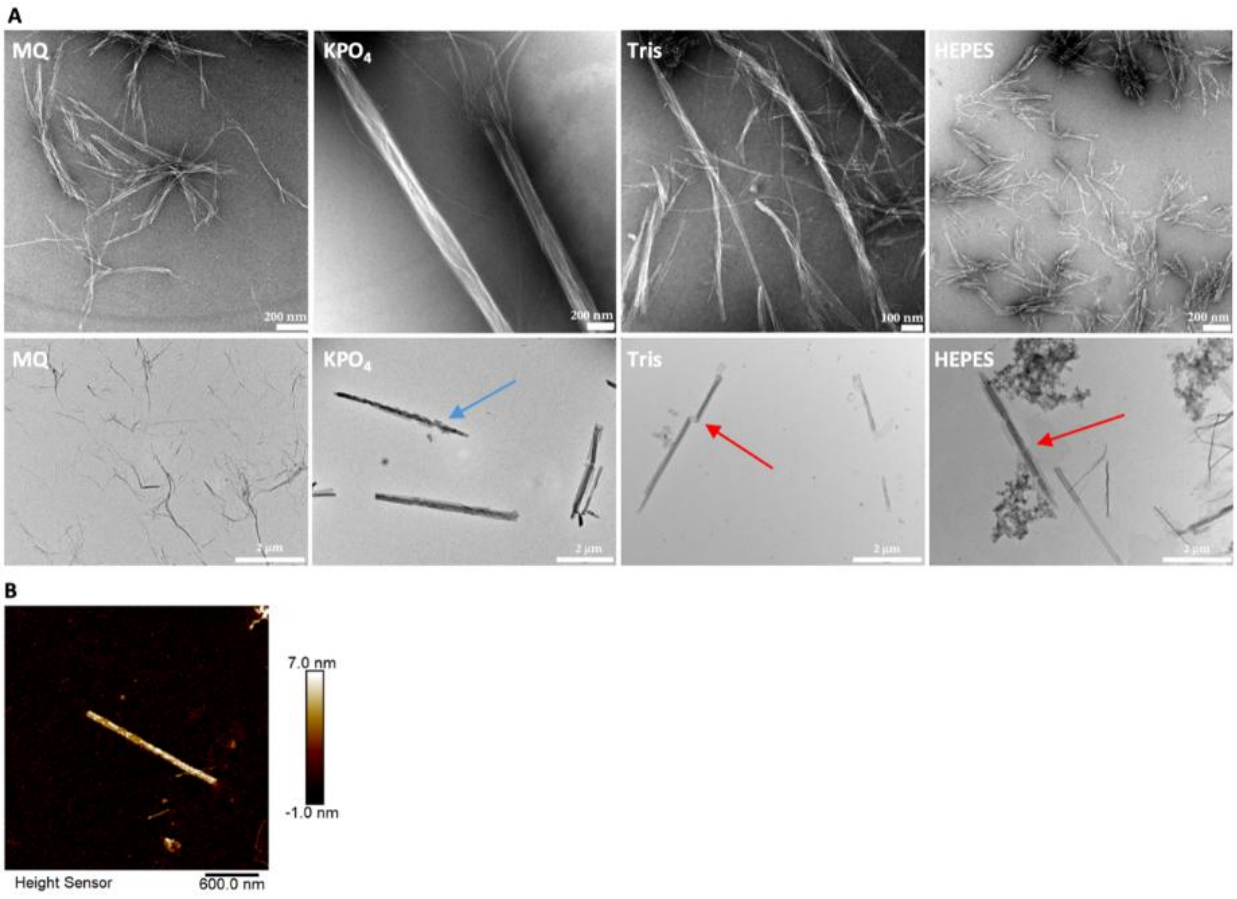


Figure 2. Morphology of aggregates of PSMα1 peptide formed in different buffers. (**A)** TEM images of the end-state fibril of PSMα1 peptide in various buffer solutions (MQ, Tris, HEPES, and KPO_4). Please note different scale bars at the micrographs. Blue arrow indicates the twisting nanotube pattern of fibrils in KPO_4, while the red arrows indicate thick fibrils wrapping around thinner ones. (**B)** Atomic-force microscopic images of end-state fibril of PSMα1 in KPO_4.

Templating of PSMα1 buffer specific aggregates through cross-seeding

The ability of fibrils with solution-specific morphologies to propagate their structural characteristics to second-generation aggregates under different solution conditions was tested using cross-seeding. Preformed fibril seeds generated in MQ-water (MQ-seeds), KPO_4 (KPO_4-seeds), Tris (Tris-seeds) and HEPES (HEPES-seeds) were introduced to monomeric PSMα1 in different solution conditions. Our findings show that cross-seeding with preformed fibril seeds accelerates the aggregation kinetics of PSMα1 and eliminates the lag phase compared to unseeded controls (Figure 3). These findings suggest that preformed fibrils provides a template for bypassing the nucleation step and directly promoting elongation[24]. Notably, unseeded PSMα1 aggregation in KPO_4 and Tris-buffer showed no detectable ThT signal due to the low peptide concentration.

SRCD analysis revealed that second-generation fibrils largely adopted the structural features of the seeds (Figure 3). In MQ-water, seeding with MQ-, KPO_4- or HEPES-derived fibrils led to aggregates that maintained β-sheet or α-helical structures matching their respective seeds. Interestingly, Tris-seeds in MQ-water produced fibrils with higher α-helical content, diverging from the β-sheet-rich structure of the Tris-seeds. These results suggest that while seeds often determine the structure of second-generation fibrils, the buffer environment can modulate or override this templating, depending on the conditions (Figure 3, Table S3).

Similar trends were observed in KPO_4 and Tris buffer, where the structural template provided by the seeds determines the assembly and structure of the new fibrils. In contrast, fibril formation in HEPES buffer varied more distinctly across all conditions. For instance, both MQ- and Tris-seeded fibrils led to increased α-helical content, deviating from their original β-sheet rich structures. Furthermore, HEPES-seeds in HEPES-buffer produced fibrils with reduced α-helical content and a shift toward unordered structures. These results suggest that in HEPES buffer, the buffer environment can override the structural influence of the seeds. Together, these findings demonstrate that while cross-seeding can effectively template the formation of second-generation fibrils, the final structures results from a dynamic interplay between the seed and the buffer environment. In most cases, the seed determines the structural outcome, but in certain environments, particularly HEPES buffer, the buffer can override the templating effect.

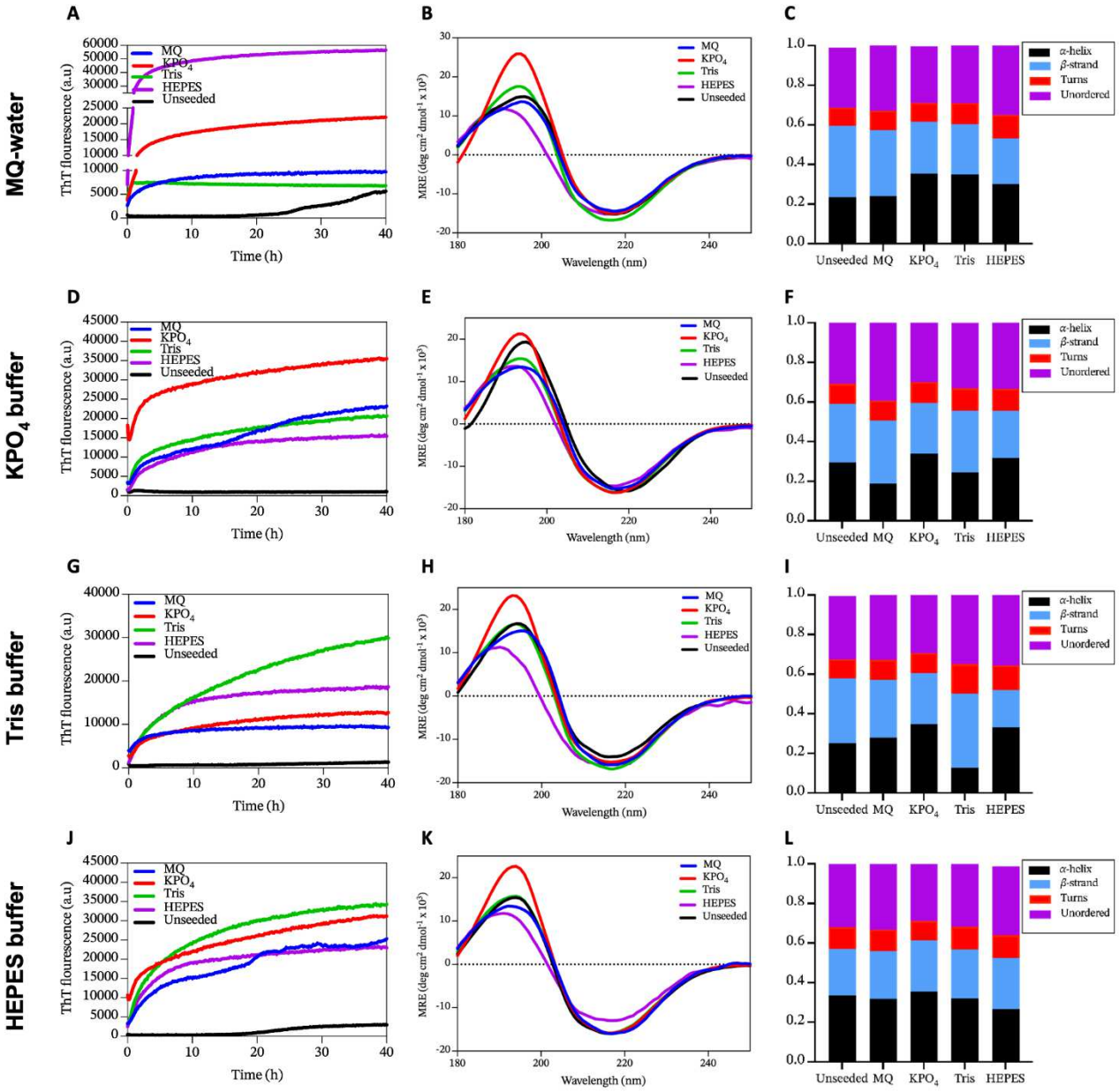


Figure 3: Cross-seeding with preformed PSMα1 fibrils from different buffers. (A) Aggregation of PSMα1 (0.5 mg/mL) in MQ-water, both in the absence and presence of 20% preformed PSMα1 seeds derived from MQ-seeds, KPO_4-seeds, Tris-seeds and HEEPES-seeds. (**B**) Structural comparison by SRCD of end-state PSMα1 fibrils formed upon seeding with MQ-seeds, KPO_4-seeds, Tris-seeds, and HEPES-seeds in MQ-water. **C**) Deconvolution of the SRCD spectra of PSMα1 fibrils formed in the presence of different seeds in MQ-water. (**D)** Aggregation of PSMα1 (0.5 mg/mL) in KPO_4, both in the absence and presence of 20% preformed PSMα1 seeds derived from MQ-seeds, KPO_4-seeds, Tris-seeds and HEEPES-seeds. (**E**) Structural comparison by SRCD of end-state PSMα1 fibrils formed upon seeding with MQ-seeds, KPO_4-seeds, Tris-seeds, and HEPES-seeds in KPO_4. (**F**) Deconvolution of the SRCD spectra of PSMα1 fibrils formed in the presence of different seeds in KPO_4. **(G)** Aggregation of PSMα1 (0.5 mg/mL) in Tris-buffer, both in the absence and presence of 20% preformed PSMα1 seeds derived from MQ-seeds, KPO_4-seeds, Tris-seeds and HEEPES-seeds. (**H**) Structural comparison by SRCD of end-state PSMα1 fibrils formed upon seeding with MQ-seeds, KPO_4-seeds, Tris-seeds, and HEPES-seeds in Tris-buffer. (**I**) Deconvolution of the SRCD spectra of PSMα1 fibrils formed in the presence of different seeds in Tris. **(J**) Aggregation of PSMα1 (0.5 mg/mL) in HEPES-buffer, both in the absence and presence of 20% preformed PSMα1 seeds derived from MQ-seeds, KPO_4-

seeds, Tris-seeds and HEEPES-seeds. (**K**) Structural comparison by SRCD of end-state PSMα1 fibrils formed upon seeding with MQ-seeds, KPO_4-seeds, Tris-seeds, and HEPES-seeds in HEPES-buffer. (**L**) Deconvolution of the SRCD spectra of PSMα1 fibrils formed in the presence of different seeds in HEPES-buffer.

Morphology of PSMα1 fibrils under different cross-seeding conditions

TEM images reveal the morphological diversity of PSMα1 fibrils formed under various cross-seeding conditions, highlighting the interplay between seed identity and buffer environment in determining fibril structure. Second-generation aggregates predominantly adopt the morphology of the seeds they were initiated with, Figure 4, emphasizing the strong templating effect of the seed, consistent with its influence on secondary structure. However, notable exceptions to this trend were observed. When KPO_4-or Tris-seeds were used in MQ-water, the resulting fibrils adopted the morphological characteristic of MQ-fibrils rather than that of the seed (Figure 4A). Similarly, MQ-seeds in KPO_4-buffer produced aggregates with the thick, ribbon-like morphology typical of KPO_4-fibrils (Figure 4B). These findings suggest that under certain conditions, specifically in MQ-water and KPO_4-buffer, the environment can override the templating effect of the seed. In contrast, in Tris and HEPES buffer, the seed consistently dictated the morphology of the resulting fibrils across all seeding conditions (Figure 4C, 4D), indicating that in these environments, the structural imprint of the seed prevails regardless of the solution conditions.

Overall, these findings reinforce the conclusion that the seed is the primary determinant of fibril morphology, mirroring its role in shaping secondary structure, although certain buffer environments can override the seed-driven templating.

Salt effect on PSMα1 aggregation

The presence of salt ions has previously been shown to impact amyloid formation for various protein including PSMα3[38]. The impact of sodium chloride (NaCl) on PSMα1 aggregation was therefore investigated focusing on the two distinct fibril morphologies formed in MQ-water and KPO_4 buffer. ThT fluorescence assays revealed that NaCl accelerated the aggregation of PSMα1 in both MQ-water and KPO_4 buffer (Figure 5A, 5B). By introducing 50 mM NaCl, the half-time decreased from 43 ± 1.1 h to 24 ± 1.1 h and at 700 mM, it was further reduced to 17 ± 0.2 h (Figure S3A, Table S4). This progressive reduction in half-time suggests that the presence of NaCl facilitates a faster onset of aggregation in MQ-water. Interestingly, when the concentration of NaCl exceeds 100 mM for PSMα1 in MQ-water the corresponding ThT curves become biphasic (Figure 5A). This could indicate the presence of intermediate species at the first plateau. In KPO_4 buffer, aggregation kinetics and half-times were generally faster than those observed in MQ-water across all NaCl concentrations (Table S4). At 0 mM NaCl, almost no ThT signal is seen corresponding to the lack of ThT signal at PSMα1 concentrations below 1 mg/mL as mentioned above. However, at 50 mM NaCl, the half-time was 17 ± 7.4 h which was faster than the corresponding condition in MQ-water. At 700 mM NaCl, the half-time in KPO_4 was further reduced to 15 ± 0.3 h, reflecting a further acceleration of the aggregation at a high NaCl concentration. At lower NaCl concentrations the half-time correlates linearly with the square root of the NaCl concentration indicating that the onset of aggregation in MQ-water is sensitive to electrostatic screening by NaCl ions (Figure 5C).

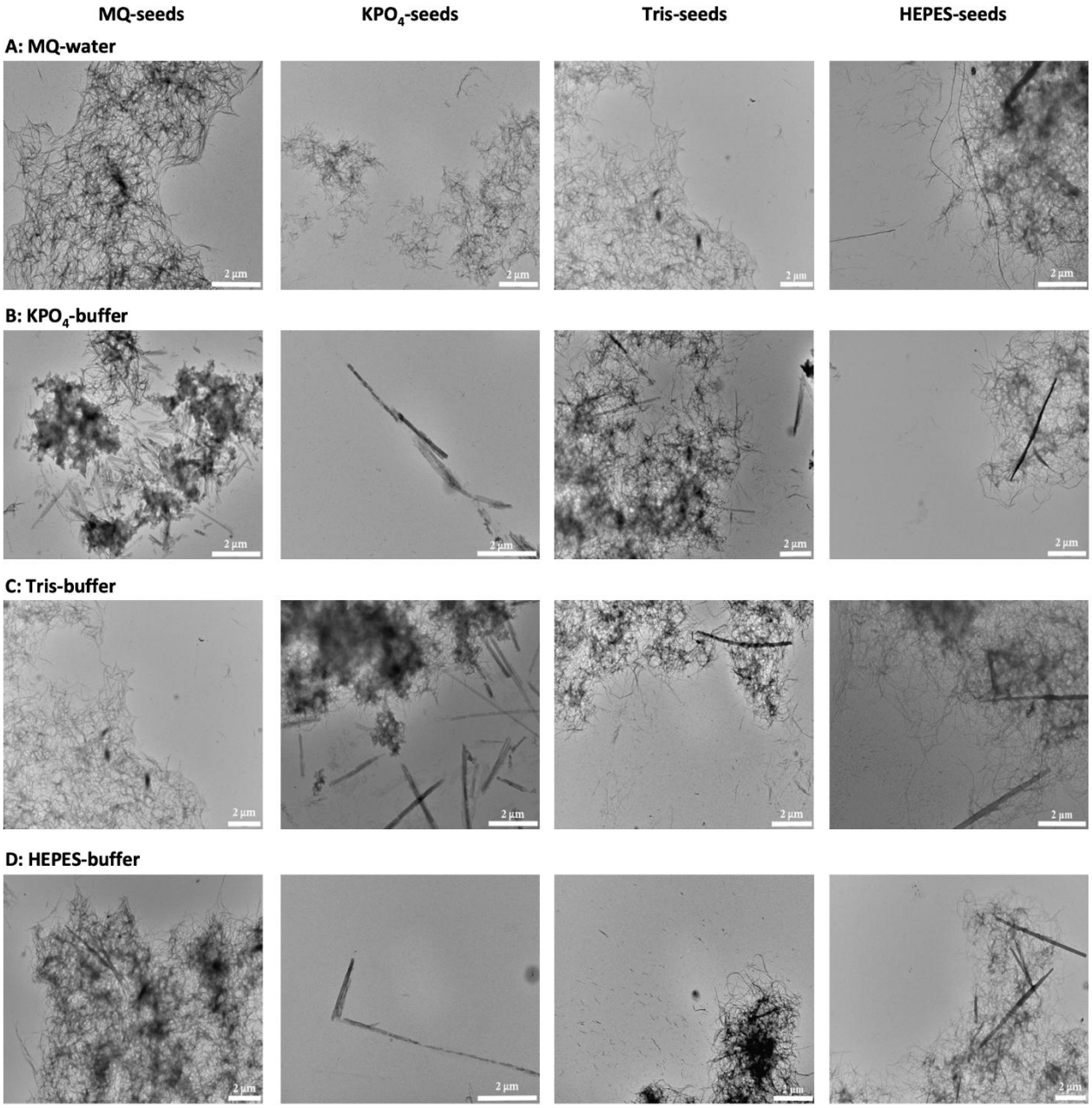


Figure 4: Morphology of PSMα1 fibrils formed in different cross-seeding conditions. (A)TEM images of the end-state fibril of PSMα1 formed upon the addition of different seeds to MQ-water. (**B**) TEM images of the end-state fibril of PSMα1 formed upon the addition of different seeds to KPO_4 buffer. (**C**) TEM images of the end-state fibril of PSMα1 formed upon the addition of different seeds in Tris buffer. (**D)** TEM images of the end-state fibril of PSMα1 formed upon the addition of different seeds to HEPES buffer.

The effect of NaCl on the surface hydrophobicity of fibrils formed in MQ-water and KPO_4 was analyzed using ANS fluorescence (Figure 5D, Figure S3B, S3C, and Table S5). In MQ-water, ANS fluorescence intensity increased with higher NaCl concentrations up to 200 mM NaCl, indicating greater exposure of hydrophobic patches on the fibril surface. The most notable increase in hydrophobicity was observed at 100 mM NaCl, and at higher salt concentrations, ANS fluorescence intensity plateaued, indicating a different fibril packing with less hydrophobic surface exposure.

Similar trends were observed in KPO_4 buffer, where the highest fluorescence peak occurred at 100 mM NaCl. However, the overall fluorescence intensities in KPO_4 buffer were consistently lower than in MQ-water, indicating that fibrils formed in KPO_4 displayed less hydrophobic residues on the surface of the fibrils. This difference may arise from variations in fibril packing or conformational states influenced by solution conditions. Fibrils formed in KPO_4 with NaCl may adopt a structure in which hydrophobic regions are less accessible to ANS binding resulting in reduced florescence intensity.

Structural changes of PSMα1 fibrils formed under different NaCl concentrations were monitored using SRCD spectroscopy (Figure 5E, 5F, and Table S6). The SRCD spectra for all fibrils formed in MQ-water at different salt concentrations revealed a predominant β-sheet structure, with a single minimum at ~217 nm for all concentrations (Figure 5E). Deconvolution of the SRCD spectra for fibrils formed in MQ-water with NaCl revealed a shift in the structural composition with increasing NaCl concentration (Figure 5G). At 0 mM NaCl fibrils displayed a mixed structural contribution comprising of 31% α-helices, 31% β-sheets, and 27% unordered structures (Table S6). As the NaCl concentration increased, the structural contribution shifted slightly towards α-helices. Fibrils formed at 50 mM, 400 mM and 700 mM NaCl contained 34%, 38% and 35% α-helices, respectively. While the proportion of β-sheets decreased slightly with increasing NaCl concentrations, the contribution from unordered structures did not significantly change with increasing NaCl concentration. Similarly, PSMα1 fibrils formed in KPO_4 buffer with various NaCl concentrations display β-sheet-rich structures, with a minimum at ~223 nm (Table S6). In KPO_4 buffer, the structural composition of fibrils exhibited a more variable picture with increasing NaCl concentrations. At 0 mM NaCl fibrils showed a balanced structural contribution, comprising of 29% α-helices, 29% β-sheets, and 29% unordered structures. A similar trend was observed in fibrils formed at 50 mM and 400 mM NaCl, with α-helices contributing with 30% and 33%, β-sheets with 36% and 34%, and unordered structures with 24% for both concentrations. However, at 700 mM NaCl, the structural composition shifted slightly with β-sheets contributing with 34%, unordered structures with 35% and α-helices with 21%.

To evaluate whether the observed structural changes translate into biological effects, LDH release assays were performed. Fibrils formed in MQ-water were significantly more cytotoxic than those formed in KPO_4 buffer, with cell death rates of ~32% and ~16%, respectively ($p<0.05$, Figure 5I). Notably, cytotoxicity was significantly increased in MQ fibrils formed at 100 mM NaCl compared to 0 mM ($p<0.05$), consistent with the structural and morphological shift observed by ANS, SRCD and TEM. In contrast, no significant difference in cytotoxicity was observed between 0 mM and 700 mM NaCl (ns, $p>0.05$), supporting that the biological effects plateaus at high salt concentrations. For KPO_4 fibrils, cytotoxicity remained unchanged across all salt concentrations (ANOVA, ns), indicating that their structural and biological profiles are less sensitive to changes in ionic strength.

Catalytic activity, assessed by nitrocefin hydrolysis, was differentially influenced by salt concentrations in MQ-water and KPO_4 buffer (Figure 5J, 5K). For MQ fibrils, catalytic activity remained relatively stable across salt concentrations, with only modest but statistically significant increases observed at 400 mM and 700 mM NaCl compared to lower concentrations ($p<0.0001$, one-way ANOVA), with 700 mM yielding the highest activity. No significant difference was observed between 0 mM and 50 mM NaCl ($p>0.05$), suggesting that MQ fibrils are generally less sensitive to changes in ionic strength in terms of catalytic function. In contrast, KPO_4-fibrils showed a different

salt-dependent response: catalytic activity peaked at 400 mM NaCl, which was significantly higher than at all other tested concentrations ($p<0.0001$). At 700 mM, catalytic activity decreased again to levels comparable to or below those at low salt concentrations, indicating a bell-shaped response to salt. These finding suggest that salt concentration modulates PSMα1 fibril catalytic activity, with KPO_4 fibrils displaying high sensitivity and optimal activity at moderate salt concentrations, while MQ fibrils maintain a relatively constant catalytic profile across a broad ionic range.

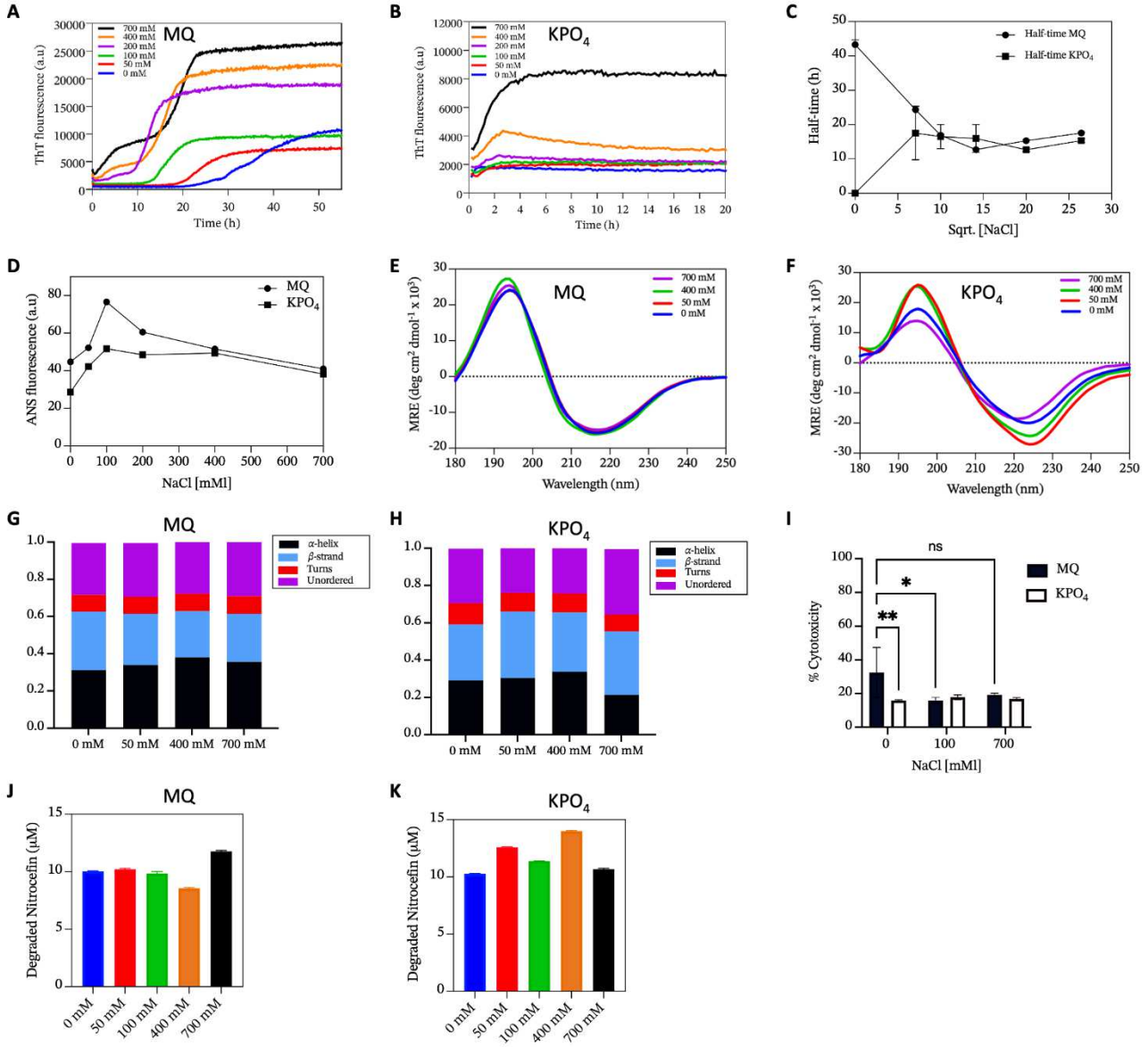


Figure 5. Effect of NaCl on PSMα1 aggregation in both MQ and KPO_4. (**A**) Aggregation kinetics of PSMα1 (0.5 mg/mL) incubated in MQ-water with 0, 50, 100, 400, or 700 mM NaCl, respectively. (**B**) Aggregation kinetics of PSMα1 (0.5 mg/mL) incubated in 10 mM KPO_4 buffer with (0, 50, 100, 400, or 700 mM NaCl, respectively. (**C**) The relationship between the halftime of fibrillation plotted against the square root of the NaCl concentration for the MQ-NaCl and KPO_4-NaCl values. (**D**) ANS fluorescens assay of PSMα1 peptide in various NaCl concentrations in MQ-water and KPO_4 buffer. **(E)** SRCD spectra of PSMα1 fibrils with NaCl in MQ. (**F**) SRCD spectra of PSMα1 aggregates with NaCl in KPO_4 buffer. **(G)** Deconvolution of the SRCD spectra of PSMα1 fibrils with NaCl in MQ. (**H**) Deconvolution of the SRCD spectra of PSMα1 fibrils with NaCl in KPO_4 buffer. **(I)** Cytotoxicity of PSMα1

fibrils with NaCl in MQ and KPO_4 buffer (*p < 0.05, **p< 0.01). **J)** Hydrolysis of nitrocefin by PSMα1 fibrils with NaCl in MQ. Statistical significance was determined using one-way ANOVA, revealing a significant difference between all solution conditions (p<0.0001). **(K)** Hydrolysis of nitrocefin by PSMα1 fibrils with NaCl in KPO_4 buffer. Statistical significance was determined using one-way ANOVA, revealing a significant difference between all solution conditions (p<0.0001).

Salt effect the morphology of PSMα1 fibrils

The morphology of PSMα1 fibrils formed under various salt concentrations was examined using TEM (Figure 6A). TEM imaging revealed notable differences in fibril morphology depending on the salt concentration. Fibrils formed in MQ-water resulted in the formation of typical thin fibrils with an average diameter of ~10 ± 3 nm (Figure 6A). At 0 mM NaCl, the fibrils were evenly distributed, but as the NaCl concentration increased, the fibrils became more bundled. At 700 mM NaCl, the fibrils assembled intro dense networks with an average diameter of ~10 ± 2 nm, accompanied with the appearance of amorphous aggregates. In contrast, fibrils formed in KPO_4 buffer exhibited a striking shift in morphology with increasing NaCl concentration (Figure 6B). At NaCl concentrations below 100 mM, thick, ribbon-like fibrils were produced, with a diameter of 121 ± 13 nm. However, as the NaCl concentration exceeded 100 mM, the morphology shifted to thin, typical PSMα1 fibrils like those observed in MQ-water in the absence of salt. At higher NaCl concentrations, amorphous aggregates were also observed in KPO_4 buffer similar to the patterns seen in MQ-water. This morphological transition aligns with changes in the secondary structure, as demonstrated by SRCD. These findings highlight the interplay between salt concentration and buffer environment in determining fibril morphology. The changes could be due to electrostatic screening, where high salt concentrations shield electrostatic repulsion between amino groups and buffer ions, preventing conformational changes.

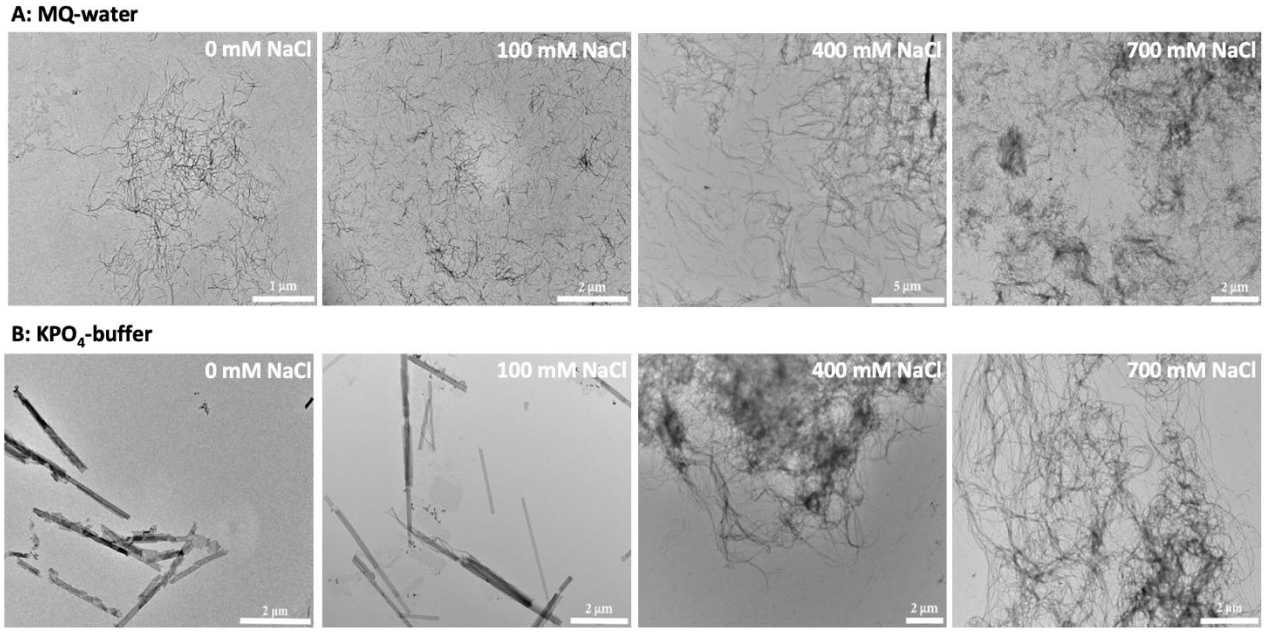


Figure 6. **Morphology of PSMα1 fibrils formed in different NaCl concentrations in MQ and KPO_4 buffer**. TEM images of the end-state fibril of PSMα1 fibrils in various NaCl concentrations (0, 100, 400 or 700 mM) in (A) MQ-water or (**B)** KPO_4 buffer. Please note that scale bar change.

Discussion

PSM peptides self-assemble into functional amyloids that are critical for biofilm integrity and key virulence factors in *S. aureus* infections[10,13,47]. While significant progress has been made in understanding the formation, structure and function of PSM amyloids, the influence of physicochemical conditions on PSMα1 aggregation remains elusive[10,24,25]. Our findings reveal that both buffer composition and salt concentration significantly modulate the aggregation kinetic, secondary structure, and morphology of PSMα1 aggregates which ultimately impact their cytotoxicity. Our results further demonstrate that varying solution conditions induce distinct structural changes in PSMα1 monomers as evidenced by SRCD spectroscopy and ANS fluorescence assay. Monomers in MQ-water and Tris buffer exhibited higher α-helical content compared to those in KPO_4 and HEPES buffers, leading to differences in hydrophobic surface exposure. These structural changes correspond to variations in hydrophobic surface exposure, a feature commonly associated with interactions at biological interfaces such as cell membranes[48]. Similar observations have been reported for other amyloid-forming proteins, including HypF-N, Aβ42 and α-synuclein, where increased hydrophobic surface exposure enhanced interactions with and disruption of cellular membranes[48]. These findings emphasize that hydrophobic surface exposure is a critical determinant of amyloid cytotoxicity. However, despite these differences in hydrophobic surface exposure, our results present a seemingly contradictory pattern. All monomers, regardless of buffer, exhibited distinct ANS fluorescence signals, indicating varying degrees of exposed hydrophobicity. Yet, the cytotoxicity of these monomers remained comparable (~20%) across all solution conditions. This suggests that structural variations alone, particularly differences in surface hydrophobicity, are insufficient to explain the observed cytotoxic effects. This contrasts with previous findings for other amyloid-forming proteins, where increased hydrophobicity correlated with higher cytotoxicity[49]. Therefore, our results imply that additional factors, beyond surface hydrophobicity, may contribute to the cytotoxic potential of PSMα1 aggregates. Interestingly, our study also revealed that monomers in KPO_4 and Tris buffers were more cytotoxic than their corresponding fibrils. This observation aligns with finding from studies on PSMα1 and PSMα3, where monomers demonstrated greater cytotoxicity than their aggregated form[10]. However, previous studies on PSMα1 monomers in MQ-water showed that the monomeric form was more cytotoxic than the corresponding fibril, which differs from our findings in MQ-water and HEPES buffer[25]. This difference may be explained by the variation in incubation time: we used two hours compared to 24 hours in the previous study[25]. For PSMα3, an increase in cytotoxicity is also observed when the peptide aggregates[10]. This enhanced cytotoxicity may be attributed to the ability of monomers to interact more readily with cellular membranes[10]. Monomers generally possess more exposed hydrophobic surfaces compared to fibrils which are more structurally stabilized and have fewer available hydrophobic surfaces to interact with cell membranes[10]. These findings suggest that the flexibility and increased membrane-interacting potential of monomers may contribute to their greater cytotoxicity relative to their aggregated forms. The buffer environment also played a significant role in determining the polymorphism of PSMα1 aggregates. The morphology of the resulting aggregates exhibited notable polymorphism with distinct variations depending on the solution used. Both HEPES and Tris buffer favored the formation of mixed thick ribbon-like fibril, thin classical fibrils, and amorphous aggregates, indicating the co-existence of potentially distinct aggregation pathways under these buffer conditions. In contrast,

KPO_4 buffer favored the formation of thick ribbon-like structures that twisted along the fibril's length, ultimately resulting in the formation of nanotubes. This is consistent with previous studies showing the formation of nanotubes in PSMα3 when incubated in Tris buffer[6]. Interestingly, despite the near-identical starting monomer conformations in HEPES and KPO_4 buffers, as indicated by their SRCD spectra, the fibrils formed in these buffers were morphologically distinct. TEM images of KPO_4 fibrils revealed predominantly thick ribbon-like structures with almost no thin fibrils and minimal amorphous aggregates. In contrast, fibrils formed in HEPES were mostly long, thin fibrils mixed with amorphous aggregates with a higher prevalence of classical thin fibrils compared to KPO_4 fibrils. The morphology of fibrils formed in HEPES buffer did not resemble those formed in KPO_4 buffer but instead shared characteristic with those formed in Tris buffer, suggesting that buffer composition has an influence on the final aggregate morphology. These observations are consistent with findings for other PSM variants, such as PSMα3 and PSMβ2, where buffers like TAPS facilitated the formation of distinct fibril morphologies, including nanotubes[37]. This variability suggests that buffer solution significantly impacts the nucleation and elongation steps during PSMα1 formation along with final fibril morphology. Polymorphic structures of PSMα1 are particularly interesting as they could have implications for biofilm resilience and bacterial pathogenicity. For instance, studies on α-synuclein have shown that structurally distinct fibrillar polymorphs can lead to different pathological outcomes such as Parkinson's disease or multiple system atrophy, depending on how different amino acid residues are exposed on the fibril surface, which influences interactions with cell membranes[30,50,51]. The stability of these polymorphs also plays a role, as more stable fibrils may be more resilient, while less stable forms could contribute to weaker biofilms, potentially making *S. aureus* more susceptible to eradication. Additionally, our study examined the cross-seeding potential of PSMα1 with pre-formed fibrils, which significantly influenced the secondary structure and morphology of the resulting aggregates. This ability of seeds to template PSMα1 aggregation highlights the inherent flexibility of PSMα1 to adopt different aggregation pathways depending on the solution conditions and cross-seeding interactions. Previous research on PSM peptides has shown that cross-seeding can accelerate PSMα1 aggregation and influence its final structure, underscoring the dynamic nature of PSM peptide interactions in biofilm formation[24].

When NaCl was introduced to the environment, it further modulated the aggregation behavior of PSMα1. At low salt concentrations in MQ-water, the fibril formation resembled the trends observed under buffer-only conditions with faster aggregation kinetics and the formation of denser fibrils. However, at higher salt concentrations, the aggregation kinetics were further accelerated, and fibril formation was markedly enhanced. A similar trend was observed in KPO_4 buffer, where increasing salt concentrations not only accelerated the aggregation kinetics but also elevated ThT fluorescence intensity, indicating a greater extent of fibril formation. In addition to modulating aggregation kinetics, the presence of NaCl in KPO_4 significantly altered the fibril morphology. At low salt concentrations (below 100 mM NaCl), the morphology predominantly consisted of thick fibrils, similar to those observed under buffer-only conditions. However, at higher salt concentrations, the morphology shifted toward thinner, classic PSMα1 fibrils. This morphological transition is consistent with previous finding for PSMα3, where low salt concentrations accelerated aggregation kinetics and produced firm, spiral fibrils, whereas high salt concentration slowed fibril formation and resulted in slim, curvilinear fibril or thin fibrils[38]. Rapid aggregation is not compatible with the formation of very

thick, well-ordered fibrils or nanotubes, which may explain why high salt concentrations promote the formation of thin fibrils[52]. These observations suggest that elevated salt concentrations diminish the influence of the buffer on aggregation pathways, likely due to the formation of an ionic shielding layer around the fibrils, as described by the Debye-Hückel screening effect. This shielding reduces electrostatic interactions between the buffer and the fibrils, leading to more uniform fibril morphology regardless of the buffer composition.

The observed sensitivity of PSMα1 aggregation to buffer and salt conditions may have profound implications for its functional role in biofilm integrity and bacterial virulence. The ability of PSMα1 to form diverse fibrillar assemblies suggests a mechanism by which *S. aureus* can adapt to different host environments, optimizing biofilm formation and resilience under varying conditions. However, the differential cytotoxicity of monomers and fibrils highlights a trade-off between maintaining biofilm integrity and minimizing host cell damage, which could be crucial for the persistence of infection.

Methods

Materials

N-terminally formylated PSMα1 peptide (>95% purity) was purchased from GenScript Biotech (Netherlands). Thioflavin T (ThT), trifluoroacetic acid (TFA), HEPES, hexafluoroisopropanol (HFIP), potassium phosphate dibasic, potassium phosphate monobasic, sodium chloride, and Tris were purchased from Sigma-Aldrich (St. Louis, MO, USA). Dimethyl sulfoxide (DMSO) and 8-Anilino-1-naphthalenesulfonic acid (ANS) were purchased from Merck (Ireland). Ultrapure water was used throughout the study. HEK293 cell line was purchased from Thermo Fisher Scientific (Waltham, MA, USA).

PSMα1 pretreatment

Lyophilized PSMα1 peptide stocks were dissolved to a concentration of 10 mg/mL in a 1:1 mixture of HFIP and TFA. The solution was sonicated using a probe sonicator (Biologics, Inc., Manassas, VA, USA) for five cycles of 20 seconds each with 30-second intervals between cycles followed by incubation at room temperature for 1 hour. The solution was then divided into 5 smaller aliquots with a concentration of 2 mg. The HFIP/TFA mixture was evaporated by Speedvac (Eppendorf Concentrator Plug, Merck, Darmstadt, Germany) at 1,000 rpm for 3 hours at room temperature. The dried stocks were stored at -70℃ until use.

Preparation of PSMα1 and buffer for kinetics experiments

Before experiments, the dried stock solutions were dissolved in 200 µL DMSO and then diluted with 800 µL of either MQ-water, HEPES, Tris or KPO_4 buffer to a concentration of 2 mg/mL. Lastly, the stock solution was passed through a 0.22 µm filter.

The buffers were prepared at a concentration of 10 mM and adjusted to a pH of 8. All buffer stock solutions were filtered using 0.45 µm syringe filters (Merck Millipore Ltd., Ireland) before use.

Kinetic experiments

All kinetic experiments were conducted using Corning clear-bottomed 96-well half-area black bottom polystyrene microtiter plates (Corning, New York, NY, USA) with a non-binding surface, in a

Fluostar Omega plate reader (BMG Labtech, Germany) at 37°C. Freshly dissolved peptides were diluted in the respective buffer, mixed with 0.04 mM ThT, and added to the wells (100 µL per well). Plates were sealed to prevent evaporation. The ThT fluorescence was recorded every 10 min with an excitation filter at 450 nm and an emission filter at 482 nm at quiescent conditions. Each sample was measured in triplicate.

Cross-seeding kinetic assay

For measuring kinetics with seeds, fibrils formed in different buffers were collected and sonicated for 3 x 10 seconds using a probe sonicator (Biologics, Inc., Manassas, VA, USA) at room temperature in low-bind Eppendorf tubes (Axygen). In the cross-seeding experiment 20% pre-formed fibril seeds (prepared in MQ-water, HEPES, Tris, and KPO_4 respectively) were added to the wells immediately before ThT measurements. ThT fluorescence was observed in the plate reader every 10 min under quiescent conditions.

Transmission electron microscopy (TEM) using Morgagni 268

Peptide samples were collected after the ThT fibrillation kinetics assay by pooling the contents of three identical wells from the plate. A 5 µL aliquot of the sample was placed on a carbon-coated formvar grid (EM resolutions, Keele, UK) and allowed to adhere for 2 min before blotting. Grids were then washed with MQ-water and negatively stained with 0.2% uranyl acetate for 2 min. After staining, the grids were washed twice with MQ-water and blotted dry with filter paper. Then they air-dried for 10 min before imaging. The samples were examined using a Morgagni 268 electron microscope (FEI Phillips, Hillsboro, OR, USA) equipped with a tungsten filament and a CCD digital camera with a resolution of 1376x1032 and operated at 80 KV. The fibril widths were measured using ImageJ (Rasband, W.S., ImageJ, U.S. National Institutes of Health, Bethesda, MD, USA). The final width was determined as the average of approximately 30 measurements taken from individual fibrils under the same conditions.

Transmission electron microscopy (TEM) using Tecnai TF20

Peptide samples were collected after the ThT fibrillation kinetics assay by pooling the contents of three identical wells from the plate. Samples were prepared by two different methods: droplet or air-dry. The fibrils formed in MQ-water and KPO_4 were prepared by the droplet method where 400-mesh copper grids with carbon film were glow-discharged for 60 seconds. Approximately 2.5 µL of PSMα1 sample was then applied to the grids and incubated for 10 seconds before side blotting with filter paper. The grids were subsequently negatively stained with (2% weight/volume) uranyl acetate for 10 seconds, followed by side blotting with filter paper. Fibrils formed in Tris and HEPES-buffer were prepared using the air-dry method. First, 400-mesh copper grids with carbon film were glow-discharged for 60 seconds. Approximately 5 µL of PSMα1 sample was then applied to the grids and incubated for 2 min before blotting away excess from the side with filter paper. Samples were then washed with 5 µL of MQ-water and excess was blotted away from the side with filter paper. The grids were subsequently stained with 5 µL 2% (weight/volume) uranyl acetate for 2 min, followed by blotting away excess from the side with filter paper. Grids were then allowed to air-dry for 10 min. The air-dry method is therefore similar to the method used for the Morgagni 286. Electron micrographs were captured using a Tecnai TF20 microscope equipped with a field emission gun

operating at 200 kV (Thermo Fisher Scientific, Waltham, MA, USA) and a TVIPS XF416 CMOS camera with a 4k resolution (TVIPS GmbH, Gauting, Germany).

Synchrotron radiation circular dichroism (SRCD) spectroscopy

SRCD spectra of PSM fibrils were collected at the AU-CD beamline of the ASTRID2 synchrotron, Aarhus University, Denmark. To remove DMSO from the aggregates, the samples were centrifuged three times at 13,000 rpm for 60 min at 10℃, and the pellets were resuspended in the same volume of MQ-water. Monomers were directly dissolved in their respective buffers. Three scans were performed at 24°C using a 0.02 cm path length cuvette except for the monomers, which were scanned using a 0.01 cm cuvette. The scans covered the wavelength range of 170 to 280 nm, with 1 nm intervals and a 2-second dwell time. All SRCD spectra were processed and subtracted from their respective averaged baseline (solution containing all components of the sample, except the protein), smoothed using a seven pt Savitzky–Golay filter, and the final SRCD spectra is expressed in mean residual ellipticity (MRE). The SRCD spectra of the different buffers and cross-seeding samples were deconvoluted using DichroWeb (Department of Crystallography, Institute of Structural and Molecular Biology, Birkbeck College, University of London, UK) to obtain the contribution from individual structural components[53,54]. Each spectrum was fitted using the analysis programs Selecon3, Contin, and CDSSTR with the SPM180 reference data set[54], and an average of the structural component contributions from the three analysis programs was used.

8-Anilino-1-naphthalenesulfonic acid (ANS) fluorescence assay

ANS was dissolved in MQ-water, filtered through a 0.45 μm filter, and its concentration was determined using a Nanodrop (Thermo Fisher Scientific, Waltham, MA, USA) with a molar extinction coefficient of 4990 M^{-1} cm^{-1} at 350 nm. Fibrils formed in either MQ-water, HEPES, Tris or KPO_4 buffer were incubated with 1 mM ANS for 30 min covered in tinfoil. ANS fluorescence spectra were measured on a Cary Eclipse fluorescence spectrophotometer (Agilent Technologies, CA, USA) with excitation and emission slit widths of 10 nm. The experiments were conducted in a black 3 mm x 10 mm Quartz cuvette at 25 °C. The excitation wavelength was set to 365 nm, and emission spectra were recorded from 400 to 600 nm. Each sample spectrum was on average three scans with an integration time of 0.1 s.

Atomic force microscopy (AFM)

The fibrillated samples were collected using the same method described in the TEM section. For preparation, a 10 μL drop of 0.5 mg/mL PSMα1 from the four different solution conditions was placed on a freshly cleaved mica substrate, incubated for 2 min, rinsed with MQ-water, and dried with N_2 gas. The surface morphology was examined using a Dimension Icon AFM system (Bruker, Billerica, MA, USA) operating in tapping mode, equipped with a scanasyst-air cantilever with a spring constant of approximately 0.4 N/m, resonance frequency ~ 70kHz, and a nominal tip radius of ~2 nm was used. Images for the statistical analysis of PSMα1 fibrils from the different solutions were captured from different areas on mica surface. NanoScope Analysis 3.0 software (Veeco Instruments Inc., NY, USA) was used for image processing, including flattening images and measuring line profiles.

Cell viability assays

Flp-In HEK293 cells (Thermo Fischer Scientific, Waltham, MA, USA) were cultured in Dulbecco's Modified Eagle's Medium (DMEM) with high glucose but without sodium pyruvate (Sigma-Aldrich, St. Louis, MO, USA). The medium was supplemented with 10% Fetal bovine serum (FBS), L-glutamine (Glu) and penicillin (100 U/mL)-streptomycin (0.1 mg/mL). Cells were maintained at 37℃ in a humidified atmosphere containing 5% CO_2 and 95% air. The fibrils used in the experiment were prepared from the ThT kinetic experiments. To remove DMSO the fibrillated samples (in triplicates) were pooled and centrifuged once at 13,000 rpm for 60 min at 15℃. Following centrifugation, the supernatant was carefully removed, and the pellets were resuspended in the original buffer to a final concentration of 100 μM. Monomers were directly dissolved in their respective buffers to a final concentration of 100 μM.

On the first day of the experiment, HEK293 cells were harvested using 2 mL TrypLE Express (Thermo Fisher, Waltham, MA, USA), resuspended in 20 mL of preheated DMEM, and centrifuged at 300xg for 5 min at 20℃. The supernatant was removed, and the cell pellet was resuspended in DMEM to a concentration of $\sim 1\times10^5$ cells/mL. Fibrils generated in the different buffers were added to the cells at a final fibril concentration of 5 μM with 10.000 cells per well. The cells had an initial viability of 97.2%. 100 μL of the cell suspension was added to each well of a clear 96-well plate (Sarstedt, Nümbrecht, Germany) and incubate overnight at 37℃. On the second day, the old media were removed, and 5 μM PSMα1 fibrils along with pre-heated DMEM were added to each well to a total volume of 75 μL. For the cytotoxicity control wells, 7.5 μ of lysis solution was added to a total volume of 75 μL. The plate was covered with a lid and incubated for two hours at 37℃. Then 68 μL of the mixture was moved to a new 96-well plate, and the cells were centrifuged at 250g for 4 min. Following centrifugation, 50 μL of the supernatant was carefully transferred to a flat, white 96-well plate (Greiner Bio-One, Kremsmünster, Austria). Next, 50 μL of CytoTox Reagent (Sigma-Aldrich, St. Louis, MO, USA) was added to each well, and then the plate was covered with tinfoil and incubated for 30 min at room temperature. After incubation, 50 μL stopping-solution was added to all wells, and the absorbance was recorded at 490 nm within one hour using Perkin Elmer EnSpire 2300 multimode plate reader (Perkin Elmer Instruments, Waltham, MA, USA). The following equation was used to calculate % cytotoxicity:

$$\%\ \text{Cytotoxicity} = 100 \cdot \frac{(\text{Experimental value} - \text{low control})}{(\text{Lysis control} - \text{low control})}$$

Statistical analysis was performed using two-way ANOVA in GraphPad Prism version 10 for Mac (GraphPad Software, Massachusetts, USA).

Nitrocefin hydrolysis assay

Nitrocefin stock solutions were dissolved in DMSO to a concentration of 5 mM and stored at -80℃ until use. The stock solutions were diluted to 90 μM using pre-cooled appropriate buffer solution (MQ-water, HEPES, Tris, and KPO_4). To minimize self-hydrolysis of nitrocefin, all solutions were pre-cooled and kept on ice throughout the experiment. For each reaction, pre-cooled buffer solutions (MQ-water, HEPES, Tris, and KPO_4) and PSMα1 samples (1 mg/mL) was mixed with nitrocefin to reach a final concentration of 60 μM nitrocefin and PSMα1 concentrations of 150, 100, 50, or 0 μM. The solution was mixed in a pre-cooled black μClear 96 well plate with a clear bottom Greiner Bio-One, Kremsmünster, Austria). The final volume in each well was 180 μL. Each condition was

prepared in triplicate. Immediately after mixing, the plate was transferred to a Perkin Elmer EnSpire 2300 multimode plate reader (Perkin Elmer Instruments, Waltham, MA, USA) set to 20℃. The absorbance of degraded nitrocefin was measured every 20 seconds for two hours at 480 nm. Data is presented as the mean of the final five absorbance measurements for each condition. Statistical analysis was performed using one-way ANOVA in GraphPad Prism version 10 for Mac (GraphPad Software, Massachusetts, USA).

Funding

This work was supported Aarhus University Research foundation NOVA (AUFF-E-2023-9-18), Magda Sofie and Aase Lütz's Memorial Trust and Hørslevfonden.

References

1 Blancas-Mejía, L. M. & Ramirez-Alvarado, M. Systemic amyloidoses. *Annu Rev Biochem* **82**, 745-774 (2013). https://doi.org:10.1146/annurev-biochem-072611-130030

2 Eisenberg, D. & Jucker, M. The Amyloid State of Proteins in Human Diseases. *Cell* **148**, 1188-1203 (2012). https://doi.org:https://doi.org/10.1016/j.cell.2012.02.022

3 Eisenberg, D. S. & Sawaya, M. R. Structural Studies of Amyloid Proteins at the Molecular Level. *Annu Rev Biochem* **86**, 69-95 (2017). https://doi.org:10.1146/annurev-biochem-061516-045104

4 Iadanza, M. G., Jackson, M. P., Hewitt, E. W., Ranson, N. A. & Radford, S. E. A new era for understanding amyloid structures and disease. *Nature Reviews Molecular Cell Biology* **19**, 755-773 (2018). https://doi.org:10.1038/s41580-018-0060-8

5 Otzen, D. & Riek, R. Functional Amyloids. *Cold Spring Harb Perspect Biol* **11** (2019). https://doi.org:10.1101/cshperspect.a033860

6 Salinas, N., Colletier, J. P., Moshe, A. & Landau, M. Extreme amyloid polymorphism in Staphylococcus aureus virulent PSMα peptides. *Nat Commun* **9**, 3512 (2018). https://doi.org:10.1038/s41467-018-05490-0

7 Maji, S. K. *et al.* Functional amyloids as natural storage of peptide hormones in pituitary secretory granules. *Science* **325**, 328-332 (2009). https://doi.org:10.1126/science.1173155

8 Majumdar, A. *et al.* Critical Role of Amyloid-like Oligomers of Drosophila Orb2 in the Persistence of Memory. *Cell* **148**, 515-529 (2012). https://doi.org:https://doi.org/10.1016/j.cell.2012.01.004

9 Dean, D. N. & Lee, J. C. Modulating functional amyloid formation via alternative splicing of the premelanosomal protein PMEL17. *Journal of Biological Chemistry* **295**, 7544-7553 (2020). https://doi.org:https://doi.org/10.1074/jbc.RA120.013012

10 Tayeb-Fligelman, E., Salinas, N., Tabachnikov, O. & Landau, M. Staphylococcus aureus PSMα3 Cross-α Fibril Polymorphism and Determinants of Cytotoxicity. *Structure* **28**, 301-313.e306 (2020). https://doi.org:10.1016/j.str.2019.12.006

11 Hansen, K. H. *et al.* Structural basis of Pseudomonas biofilm-forming functional amyloid FapC formation. *Science Advances* **11**, eadx7829 (2025). https://doi.org:doi:10.1126/sciadv.adx7829

12 Hansen, K. H. *et al.* Structure of biofilm-forming functional amyloid PSMα1 from Staphylococcus aureus. *Proceedings of the National Academy of Sciences* **121**, e2406775121 (2024). https://doi.org:doi:10.1073/pnas.2406775121
13 Schwartz, K., Syed, A. K., Stephenson, R. E., Rickard, A. H. & Boles, B. R. Functional amyloids composed of phenol soluble modulins stabilize Staphylococcus aureus biofilms. *PLoS Pathog* **8**, e1002744 (2012). https://doi.org:10.1371/journal.ppat.1002744
14 Otto, M. Staphylococcal biofilms. *Curr Top Microbiol Immunol* **322**, 207-228 (2008). https://doi.org:10.1007/978-3-540-75418-3_10
15 Otto, M. Phenol-soluble modulins. *Int J Med Microbiol* **304**, 164-169 (2014). https://doi.org:10.1016/j.ijmm.2013.11.019
16 Wang, R. *et al.* Identification of novel cytolytic peptides as key virulence determinants for community-associated MRSA. *Nature Medicine* **13**, 1510-1514 (2007). https://doi.org:10.1038/nm1656
17 Surewaard, B. G. *et al.* Staphylococcal alpha-phenol soluble modulins contribute to neutrophil lysis after phagocytosis. *Cell Microbiol* **15**, 1427-1437 (2013). https://doi.org:10.1111/cmi.12130
18 Cogen, A. L. *et al.* Selective antimicrobial action is provided by phenol-soluble modulins derived from Staphylococcus epidermidis, a normal resident of the skin. *J Invest Dermatol* **130**, 192-200 (2010). https://doi.org:10.1038/jid.2009.243
19 Joo, H.-S., Cheung, G. Y. C. & Otto, M. Antimicrobial Activity of Community-associated Methicillin-resistant Staphylococcus aureus Is Caused by Phenol-soluble Modulin Derivatives *. *Journal of Biological Chemistry* **286**, 8933-8940 (2011). https://doi.org:10.1074/jbc.M111.221382
20 Rigby, K. M. & DeLeo, F. R. Neutrophils in innate host defense against Staphylococcus aureus infections. *Semin Immunopathol* **34**, 237-259 (2012). https://doi.org:10.1007/s00281-011-0295-3
21 Nielsen, A. *et al.* Solonamide B inhibits quorum sensing and reduces Staphylococcus aureus mediated killing of human neutrophils. *PLoS One* **9**, e84992 (2014). https://doi.org:10.1371/journal.pone.0084992
22 Bleem, A., Francisco, R., Bryers, J. D. & Daggett, V. Designed α-sheet peptides suppress amyloid formation in Staphylococcus aureus biofilms. *npj Biofilms and Microbiomes* **3**, 16 (2017). https://doi.org:10.1038/s41522-017-0025-2
23 Arad, E. *et al.* Staphylococcus aureus functional amyloids catalyze degradation of β-lactam antibiotics. *Nature Communications* **14**, 8198 (2023). https://doi.org:10.1038/s41467-023-43624-1
24 Zaman, M. & Andreasen, M. Cross-talk between individual phenol-soluble modulins in Staphylococcus aureus biofilm enables rapid and efficient amyloid formation. *eLife* **9**, e59776 (2020). https://doi.org:10.7554/eLife.59776
25 Hansen, K. H. *et al.* Structure of biofilm-forming functional amyloid PSMα1 from Staphylococcus aureus. *Proc Natl Acad Sci U S A* **121**, e2406775121 (2024). https://doi.org:10.1073/pnas.2406775121
26 Meinhardt, J., Sachse, C., Hortschansky, P., Grigorieff, N. & Fändrich, M. Abeta(1-40) fibril polymorphism implies diverse interaction patterns in amyloid fibrils. *J Mol Biol* **386**, 869-877 (2009). https://doi.org:10.1016/j.jmb.2008.11.005

27 Jiménez, J. L. *et al.* The protofilament structure of insulin amyloid fibrils. *Proc Natl Acad Sci U S A* **99**, 9196-9201 (2002). https://doi.org:10.1073/pnas.142459399
28 Annamalai, K. *et al.* Polymorphism of Amyloid Fibrils In Vivo. *Angew Chem Int Ed Engl* **55**, 4822-4825 (2016). https://doi.org:10.1002/anie.201511524
29 Close, W. *et al.* Physical basis of amyloid fibril polymorphism. *Nature Communications* **9**, 699 (2018). https://doi.org:10.1038/s41467-018-03164-5
30 Tycko, R. Amyloid polymorphism: structural basis and neurobiological relevance. *Neuron* **86**, 632-645 (2015). https://doi.org:10.1016/j.neuron.2015.03.017
31 Madine, J. *et al.* Structural insights into the polymorphism of amyloid-like fibrils formed by region 20-29 of amylin revealed by solid-state NMR and X-ray fiber diffraction. *J Am Chem Soc* **130**, 14990-15001 (2008). https://doi.org:10.1021/ja802483d
32 Frey, L. *et al.* On the pH-dependence of α-synuclein amyloid polymorphism and the role of secondary nucleation in seed-based amyloid propagation. *eLife* **12**, RP93562 (2024). https://doi.org:10.7554/eLife.93562
33 Lövestam, S. *et al.* Disease-specific tau filaments assemble via polymorphic intermediates. *Nature* **625**, 119-125 (2024). https://doi.org:10.1038/s41586-023-06788-w
34 Eichner, T. & Radford, S. E. A diversity of assembly mechanisms of a generic amyloid fold. *Mol Cell* **43**, 8-18 (2011). https://doi.org:10.1016/j.molcel.2011.05.012
35 Kameoka, D., Masuzaki, E., Ueda, T. & Imoto, T. Effect of buffer species on the unfolding and the aggregation of humanized IgG. *J Biochem* **142**, 383-391 (2007). https://doi.org:10.1093/jb/mvm145
36 Salis, A., Cappai, L., Carucci, C., Parsons, D. F. & Monduzzi, M. Specific Buffer Effects on the Intermolecular Interactions among Protein Molecules at Physiological pH. *J Phys Chem Lett* **11**, 6805-6811 (2020). https://doi.org:10.1021/acs.jpclett.0c01900
37 Kreutzberger, M. A. B. *et al.* Phenol-soluble modulins PSMα3 and PSMβ2 form nanotubes that are cross-α amyloids. *Proc Natl Acad Sci U S A* **119**, e2121586119 (2022). https://doi.org:10.1073/pnas.2121586119
38 Xuan, Q. *et al.* Salt-Inducing Assembly Polymorphism Strategy for Cytotoxicity Differentiation of Phenol-Soluble Modulin α3 Assemblies. *Biomacromolecules* **23**, 3318-3328 (2022). https://doi.org:10.1021/acs.biomac.2c00431
39 Ziaunys, M., Sakalauskas, A., Mikalauskaite, K. & Smirnovas, V. Polymorphism of Alpha-Synuclein Amyloid Fibrils Depends on Ionic Strength and Protein Concentration. *Int J Mol Sci* **22** (2021). https://doi.org:10.3390/ijms222212382
40 Kodali, R., Williams, A. D., Chemuru, S. & Wetzel, R. Abeta(1-40) forms five distinct amyloid structures whose beta-sheet contents and fibril stabilities are correlated. *J Mol Biol* **401**, 503-517 (2010). https://doi.org:10.1016/j.jmb.2010.06.023
41 Paravastu, A. K., Qahwash, I., Leapman, R. D., Meredith, S. C. & Tycko, R. Seeded growth of beta-amyloid fibrils from Alzheimer's brain-derived fibrils produces a distinct fibril structure. *Proc Natl Acad Sci U S A* **106**, 7443-7448 (2009). https://doi.org:10.1073/pnas.0812033106
42 Zhou, J. *et al.* Environmental Control of Amyloid Polymorphism by Modulation of Hydrodynamic Stress. *ACS Nano* **15**, 944-953 (2021). https://doi.org:10.1021/acsnano.0c07570
43 Nekooki-Machida, Y. *et al.* Distinct conformations of in vitro and in vivo amyloids of huntingtin-exon1 show different cytotoxicity. *Proc Natl Acad Sci U S A* **106**, 9679-9684 (2009). https://doi.org:10.1073/pnas.0812083106

44 Goto, Y. & Fink, A. L. Conformational states of beta-lactamase: molten-globule states at acidic and alkaline pH with high salt. *Biochemistry* **28**, 945-952 (1989). https://doi.org:10.1021/bi00429a004
45 Towle, K. M. *et al.* Solution Structures of Phenol-Soluble Modulins α1, α3, and β2, Virulence Factors from Staphylococcus aureus. *Biochemistry* **55**, 4798-4806 (2016). https://doi.org:10.1021/acs.biochem.6b00615
46 Arad, E. *et al.* Staphylococcus aureus functional amyloids catalyze degradation of β-lactam antibiotics. *Nat Commun* **14**, 8198 (2023). https://doi.org:10.1038/s41467-023-43624-1
47 Zaman, M. & Andreasen, M. Modulating Kinetics of the Amyloid-Like Aggregation of S. aureus Phenol-Soluble Modulins by Changes in pH. *Microorganisms* **9** (2021). https://doi.org:10.3390/microorganisms9010117
48 Limbocker, R. *et al.* Characterization of Pairs of Toxic and Nontoxic Misfolded Protein Oligomers Elucidates the Structural Determinants of Oligomer Toxicity in Protein Misfolding Diseases. *Acc Chem Res* **56**, 1395-1405 (2023). https://doi.org:10.1021/acs.accounts.3c00045
49 Yoshiike, Y., Akagi, T. & Takashima, A. Surface structure of amyloid-beta fibrils contributes to cytotoxicity. *Biochemistry* **46**, 9805-9812 (2007). https://doi.org:10.1021/bi700455c
50 Shrivastava, A. N. *et al.* Differential Membrane Binding and Seeding of Distinct α-Synuclein Fibrillar Polymorphs. *Biophys J* **118**, 1301-1320 (2020). https://doi.org:10.1016/j.bpj.2020.01.022
51 Guerrero-Ferreira, R. *et al.* Two new polymorphic structures of human full-length alpha-synuclein fibrils solved by cryo-electron microscopy. *Elife* **8** (2019). https://doi.org:10.7554/eLife.48907
52 Andreasen, M. *et al.* Polymorphic fibrillation of the destabilized fourth fasciclin-1 domain mutant A546T of the Transforming growth factor-β-induced protein (TGFBIp) occurs through multiple pathways with different oligomeric intermediates. *J Biol Chem* **287**, 34730-34742 (2012). https://doi.org:10.1074/jbc.M112.379552
53 Whitmore, L. & Wallace, B. A. DICHROWEB, an online server for protein secondary structure analyses from circular dichroism spectroscopic data. *Nucleic Acids Res* **32**, W668-673 (2004). https://doi.org:10.1093/nar/gkh371
54 Whitmore, L. & Wallace, B. A. Protein secondary structure analyses from circular dichroism spectroscopy: methods and reference databases. *Biopolymers* **89**, 392-400 (2008). https://doi.org:10.1002/bip.20853

Data availability

Data for this article, including kinetic data, synchrotron radiation circular dichroism data, cell cytotoxicity data nitrocefin hydrolysis data, and ANS fluorescence data are available at FigShare at DOI: 10.6084/m9.figshare.30464852 or https://figshare.com/account/items/30464852.

Author contributions

Writing – original draft; E.B.P., Ü.A. and M.A. Performed research; E.B.P., K.H.H. and Q.L. Analysed data; E.B.P, Q.L. and M.A. Resources; M.A. and Ü.A. Writing – review; E.B.P, K.H.H., Q.L., Ü.A. and M.A.

Acknowledgments

This work was supported Aarhus University Research foundation NOVA (AUFF-E-2023-9-18), Magda Sofie and Aase Lütz's Memorial Trust and Hørslevfonden. We acknowledge the award of beam time on the AU-CD beam line at ASTRID2 and University of Pittsburgh School of Medicine (UPSOM) for access to the TEM facilities. We thank Maria Pauladòttir Jensen and Anders Etzerodt for their help in HEK293 cell cultures.

Competing interest

The authors declare no conflict of interest.

Figure Legends

Figure 1. Solution conditions affect the aggregation kinetics and structural properties of the aggregates formed. (**A**) ThT fluorescence aggregation kinetics of PSMα1peptides (1 mg/mL) in different solutions (HEPES, Tris, KPO_4, and MQ-water) under quiescent conditions. (**B**). Left y-axis: ANS fluorescence of PSMα1fibrils in different buffer environments. Right y-axis: ANS fluorescence of PSMα1 monomers in different buffer environments. (**C**) Synchrotron radiation (SR) far UV-CD spectra of PSMα1 monomers in various buffers. (**D)** Synchrotron radiation (SR) far UV-CD spectra of PSMα1 fibrils in various buffers. (**E**) Deconvolution of the SRCD spectra of PSMα1 monomers and fibrils formed in different solutions. (**F**) Cytotoxicity of PSMα1 monomers and fibrils in different solutions. Statistical significance was determined using two-way ANOVA. *$p < 0.05$, **$p< 0.01$ (**G)** Hydrolysis of nitrocefin by PSMα1 fibrils from different solution conditions. Statistical significance was determined using one-way ANOVA, revealing a significant difference between all solution conditions ($p<0.0001$).

Figure 2. Morphology of aggregates of PSMα1 peptide formed in different buffers. (**A)** TEM images of the end-state fibril of PSMα1 peptide in various buffer solutions (MQ, Tris, HEPES, and KPO_4). Please note different scale bars at the micrographs. Blue arrow indicates the twisting nanotube pattern of fibrils in KPO_4, while the red arrows indicate thick fibrils wrapping around thinner ones. (**B)** Atomic-force microscopic images of end-state fibril of PSMα1 in KPO_4.

Figure 3: Cross-seeding with preformed PSMα1 fibrils from different buffers. (A) Aggregation of PSMα1 (0.5 mg/mL) in MQ-water, both in the absence and presence of 20% preformed PSMα1 seeds derived from MQ-seeds, KPO_4-seeds, Tris-seeds and HEEPES-seeds. (**B**) Structural comparison by SRCD of end-state PSMα1 fibrils formed upon seeding with MQ-seeds, KPO_4-seeds, Tris-seeds, and HEPES-seeds in MQ-water. **C**) Deconvolution of the SRCD spectra of PSMα1 fibrils formed in the presence of different seeds in MQ-water. (**D)** Aggregation of PSMα1 (0.5 mg/mL) in KPO_4, both in the absence and presence of 20% preformed PSMα1 seeds derived from MQ-seeds, KPO_4-seeds, Tris-seeds and HEEPES-seeds. (**E**) Structural comparison by SRCD of end-state PSMα1 fibrils formed upon seeding with MQ-seeds, KPO_4-seeds, Tris-seeds, and HEPES-seeds in KPO_4. (**F**) Deconvolution of the SRCD spectra of PSMα1 fibrils formed in the presence of different seeds in KPO_4. **(G**) Aggregation of PSMα1 (0.5 mg/mL) in Tris-buffer, both in the absence and presence of 20% preformed PSMα1 seeds derived from MQ-seeds, KPO_4-seeds, Tris-seeds and

HEEPES-seeds. (**H**) Structural comparison by SRCD of end-state PSMα1 fibrils formed upon seeding with MQ-seeds, KPO_4-seeds, Tris-seeds, and HEPES-seeds in Tris-buffer. (**I**) Deconvolution of the SRCD spectra of PSMα1 fibrils formed in the presence of different seeds in Tris. **(J**) Aggregation of PSMα1 (0.5 mg/mL) in HEPES-buffer, both in the absence and presence of 20% preformed PSMα1 seeds derived from MQ-seeds, KPO_4-seeds, Tris-seeds and HEEPES-seeds. (**K**) Structural comparison by SRCD of end-state PSMα1 fibrils formed upon seeding with MQ-seeds, KPO_4-seeds, Tris-seeds, and HEPES-seeds in HEPES-buffer. (**L**) Deconvolution of the SRCD spectra of PSMα1 fibrils formed in the presence of different seeds in HEPES-buffer.

Figure 4: Morphology of PSMα1 fibrils formed in different cross-seeding conditions. (A)TEM images of the end-state fibril of PSMα1 formed upon the addition of different seeds to MQ-water. (**B**) TEM images of the end-state fibril of PSMα1 formed upon the addition of different seeds to KPO_4 buffer. (**C**) TEM images of the end-state fibril of PSMα1 formed upon the addition of different seeds in Tris buffer. (**D)** TEM images of the end-state fibril of PSMα1 formed upon the addition of different seeds to HEPES buffer.

Figure 5. Effect of NaCl on PSMα1 aggregation in both MQ and KPO_4. (**A**) Aggregation kinetics of PSMα1 (0.5 mg/mL) incubated in MQ-water with 0, 50, 100, 400, or 700 mM NaCl, respectively. (**B**) Aggregation kinetics of PSMα1 (0.5 mg/mL) incubated in 10 mM KPO_4 buffer with (0, 50, 100, 400, or 700 mM NaCl, respectively. (**C**) The relationship between the halftime of fibrillation plotted against the square root of the NaCl concentration for the MQ-NaCl and KPO_4-NaCl values. (**D**) ANS fluorescens assay of PSMα1 peptide in various NaCl concentrations in MQ-water and KPO_4 buffer. **(E)** SRCD spectra of PSMα1 fibrils with NaCl in MQ. (**F**) SRCD spectra of PSMα1 aggregates with NaCl in KPO_4 buffer. (**G)** Deconvolution of the SRCD spectra of PSMα1 fibrils with NaCl in MQ. (**H**) Deconvolution of the SRCD spectra of PSMα1 fibrils with NaCl in KPO_4 buffer. **(I)** Cytotoxicity of PSMα1 fibrils with NaCl in MQ and KPO_4 buffer (*$p < 0.05$, **$p< 0.01$). **J)** Hydrolysis of nitrocefin by PSMα1 fibrils with NaCl in MQ. Statistical significance was determined using one-way ANOVA, revealing a significant difference between all solution conditions ($p<0.0001$). **(K)** Hydrolysis of nitrocefin by PSMα1 fibrils with NaCl in KPO_4 buffer. Statistical significance was determined using one-way ANOVA, revealing a significant difference between all solution conditions ($p<0.0001$).

Figure 6. **Morphology of PSMα1 fibrils formed in different NaCl concentrations in MQ and KPO_4 buffer**. TEM images of the end-state fibril of PSMα1 fibrils in various NaCl concentrations (0, 100, 400 or 700 mM) in (A) MQ-water or (**B)** KPO_4 buffer. Please note that scale bar change.

Supplementary Files

This is a list of supplementary files associated with this preprint. Click to download.

- Supplementaryinformation.docx